ADVANCED MATERIALS
www.advmat.de

Minimizing Interfacial Recombination in 1.8 eV Triple-Halide Perovskites for 27.5% Efficient All-Perovskite Tandems

Fengjiu Yang, Philipp Tockhorn, Artem Musiienko, Felix Lang, Dorothee Menzel, Rowan Macqueen, Eike Köhnen, Ke Xu, Silvia Mariotti, Daniele Mantione, Lena Merten, Alexander Hinderhofer, Bor Li, Dan R. Wargulski, Steven P. Harvey, Jiahuan Zhang, Florian Scheler, Sebastian Berwig, Marcel Roß, Jarla Thiesbrummel, Amran Al-Ashouri, Kai O. Brinkmann, Thomas Riedl, Frank Schreiber, Daniel Abou-Ras, Henry Snaith, Dieter Neher, Lars Korte, Martin Stolterfoht, and Steve Albrecht**

All-perovskite tandem solar cells show great potential to enable the highest performance at reasonable costs for a viable market entry in the near future. In particular, wide-bandgap (WBG) perovskites with higher open-circuit voltage (V_{OC}) are essential to further improve the tandem solar cells' performance. Here, a new 1.8 eV bandgap triple-halide perovskite composition in conjunction with a piperazinium iodide (PI) surface treatment is developed. With structural analysis, it is found that the PI modifies the surface through a reduction of excess lead iodide in the perovskite and additionally penetrates the bulk. Constant light-induced magneto-transport measurements are applied to separately resolve charge carrier properties of electrons and holes. These measurements reveal a reduced deep trap state density, and improved steady-state carrier lifetime (factor 2.6) and diffusion lengths (factor 1.6). As a result, WBG PSCs achieve 1.36 V V_{OC}, reaching 90% of the radiative limit. Combined with a 1.26 eV narrow bandgap (NBG) perovskite with a rubidium iodide additive, this enables a tandem cell with a certified scan efficiency of 27.5%.

1. Introduction

Metal-halide perovskites have raised great interest for the application in tandem solar cells since they offer the ability to greatly exceed the efficiency of today's incumbent photovoltaics (PVs) technologies, which are based on single junctions of silicon (Si), or thin-film semiconductors. One of the key features of perovskites is that the bandgap can be tuned through composition engineering.[1–3] Choosing an optimum combination of bandgaps allows to efficiently utilize sunlight in two (or more) absorber layers, such as in the combination of perovskite/Si,[4–6] perovskite/CIGS (copper indium gallium selenide),[7–9] perovskite/organic,[10–12] and perovskite/perovskite[13–30] tandem solar cells. Particularly, all-perovskite tandems are of great interest since they have the

F. Yang, P. Tockhorn, A. Musiienko, D. Menzel, R. Macqueen, E. Köhnen, K. Xu, S. Mariotti, B. Li, D. R. Wargulski, J. Zhang, F. Scheler, S. Berwig, M. Roß, A. Al-Ashouri, D. Abou-Ras, L. Korte, S. Albrecht
Division Solar Energy
Helmholtz-Zentrum Berlin für Materialien und Energie GmbH
12489 Berlin, Germany
E-mail: fengjiu.yang@nrel.gov; steve.albrecht@helmholtz-berlin.de

F. Yang
National Renewable Energy Laboratory
Golden, Colorado 80401, USA

The ORCID identification number(s) for the author(s) of this article can be found under https://doi.org/10.1002/adma.202307743

DOI: 10.1002/adma.202307743

F. Lang, D. Neher, M. Stolterfoht
Institute of Physics and Astronomy
University of Potsdam
14476 Potsdam-Golm, Germany

D. Mantione
POLYMAT
University of the Basque Country UPV/EHU
Av. Tolosa 72, Donostia-San Sebastián 20018, Spain

D. Mantione
IKERBASQUE
Basque Foundation for Science
Bilbao 48009, Spain

D. Mantione
POLYKEY s.l.
Av. Tolosa 72, Donostia-San Sebastián 20018, Spain

potential to be manufactured at lower costs and CO_2 emissions than silicon-containing tandem technologies.[31] Typically, an all-perovskite tandem solar cell (APTSC) combines a narrow-bandgap (NBG, ≈1.25 eV) mixed tin-lead (Sn-Pb) perovskite for the bottom cell, and a wide-bandgap (WBG, ≈1.8 eV) lead (Pb) perovskite for the top cell.[13–15,19,26,27,29,32–35] The highest certified power conversion efficiency (PCE) of APTSC is 29.1%, which largely surpasses the best single-junction perovskite solar cells (PSCs, 26.1% PCE).[36,37] In addition, the PCE of all-perovskite tandems increased rapidly over the last years due to significant improvements in the NBG Sn-Pb perovskite subcell. This originates from combined research efforts to improve crystallinity, suppress the oxidation of Sn^{2+}, increase carrier lifetime and diffusion length, and reduce trap density by employing a close-space annealing strategy,[16] passivating molecules,[25,38] and additives' application.[14,26,27,32,39–44]

On the other hand, the performance of WBG top cells has to be improved, as these cells face significant recombination losses due to halide-segregation, composition- and bromide (Br)-related defects, and non-ideal contact layers.[2,45,46] In addition, there are pronounced non-radiative recombination losses at the interface of the perovskite with electron transport materials (ETMs, such as fullerene-C_{60}) that can reduce the V_{OC} of WBG PSCs even further, especially for bandgaps above 1.7 eV.[47] Post-treatment of perovskite surfaces has been demonstrated as an effective approach to reduce non-radiative recombination losses and achieve higher V_{OC}.[21,48,49] Despite these efforts, most reported V_{OC}s of WBG PSCs are still below 90% of the radiative limit for bandgaps ≈1.80 eV, lagging behind the performance of perovskites with bandgaps of 1.5–1.6 eV, which reach over 95% of the radiative limit.[50]

L. Merten, A. Hinderhofer, F. Schreiber
Institute of Applied Physics
University of Tübingen
72076 Tübingen, Germany

S. P. Harvey
Materials, Chemical and Computational Sciences (MCCS)
National Renewable Energy Laboratory
Golden, CO 80401, USA

J. Thiesbrummel, H. Snaith
Clarendon Laboratory
Department of Advanced Materials and Interfaces for Photovoltaic Solar Cells
University of Oxford
Parks Road, Oxford OX1 3PU, UK

K. O. Brinkmann, T. Riedl
Institute of Electronic Devices
University of Wuppertal
42119 Wuppertal, Germany

K. O. Brinkmann, T. Riedl
Wuppertal Center for Smart Materials & Systems
University of Wuppertal
42119 Wuppertal, Germany

M. Stolterfoht
Electronic Engineering Department
The Chinese University of Hong Kong
Hong Kong SAR, China

S. Albrecht
Faculty of Electrical Engineering and Computer Science
Technische Universität Berlin
Berlin Germany

2. Results and Discussion

In this work, we developed a 1.80 eV triple-halide WBG-perovskite with piperazinium iodide (PI) as a surface treatment.[50] Our study expands on our recent work[51] on PI applied to perovskite in perovskite/silicon tandem solar cells and deepens the understanding of the PI working mechanism. We find that PI is also exceptionally well suited to reduce non-radiative recombination losses for perovskites with a bandgap of 1.8 eV. With this approach, we reduced excessive lead iodide in the perovskite film, achieved lower non-radiative recombination losses, and increased carrier lifetime. In addition, we study the charge carrier dynamics, with constant light-induced magneto-transport (CLIMAT)[52,53] measurements to resolve fingerprints of free electrons and holes separately and find that the PI treatment increases the steady-state carrier lifetime and diffusion lengths under one-sun illumination by a factor of 2.6 and 1.6, respectively. Quasi-Fermi level splitting (QFLS) analysis demonstrated that PI entirely eliminated recombination losses at the modified perovskite/C_{60} interface, reaching 1.45 eV, which marks a significant improvement over the reference (1.37 eV). The PI-modified PSC achieved a maximum PCE of 20.3% (V_{OC}: 1.34 V) and a maximum V_{OC} of 1.36 V (PCE: 20.0%), which is equal to 90% of the radiative limit, being among the highest V_{OC} for a WBG perovskite that can be integrated as the top cell in APTSCs. Combining this superior WBG PSC with an NBG Sn-Pb perovskite which utilizes rubidium iodide additive, we achieved a tandem cell with a certified efficiency of 27.5% and 27.2% maximum power point (MPP) tracked efficiency. Furthermore, as evidenced through absolute PL measurements, the potential PCE of these tandems was 30.4% with a V_{OC} potential of 2.18 V.k.

2.1. Wide-Bandgap Perovskite Study

We developed a triple halide WBG perovskite composition with a bandgap of 1.80 eV, suitable for integration into all-perovskite tandem solar cells.[55,56] For this, we determined bandgap, photovoltaic performance, and QFLS for different variations of Br (15% to 30%), and Cl contents (5% to 10%). As reported by Xu et al., perovskite compositions comprising I, Br, and Cl show a non-monotonous development of the bandgap in response to variations at the X-site[56] and therefore require a careful optimization, as detailed in Note I and Figures S1–S3 (Supporting Information). In all cases, a self-assembled monolayer (2-(9H-cabazol-9-yl)ethyl)phosphonic acid (2PACz) was employed as the hole transport material (HTM). After optimization, we selected triple-halide perovskite with a bandgap of 1.80 eV and a composition of $FA_{0.78}Cs_{0.22}Pb(Br_{0.3}I_{0.7})_3$ + 10%$MAPbCl_3$.

To further improve the V_{OC} of the WBG PSCs, we post-treated the annealed WBG perovskite with the spin-coated ionic liquid piperazinium iodide (PI), following a previously reported procedure.[50,51] This leads to a significant alteration of the perovskite surface and of the selected film properties as we describe below. In addition, the PI molecule may interact with the perovskite surface via its different surface terminating ends, potentially passivating different defects such as vacancy defects (such as V_I and V_{MA}/V_{FA}) forming undercoordinated Pb^{2+} and halide sites.[50,57] Different PI concentrations, ranging from 0.5

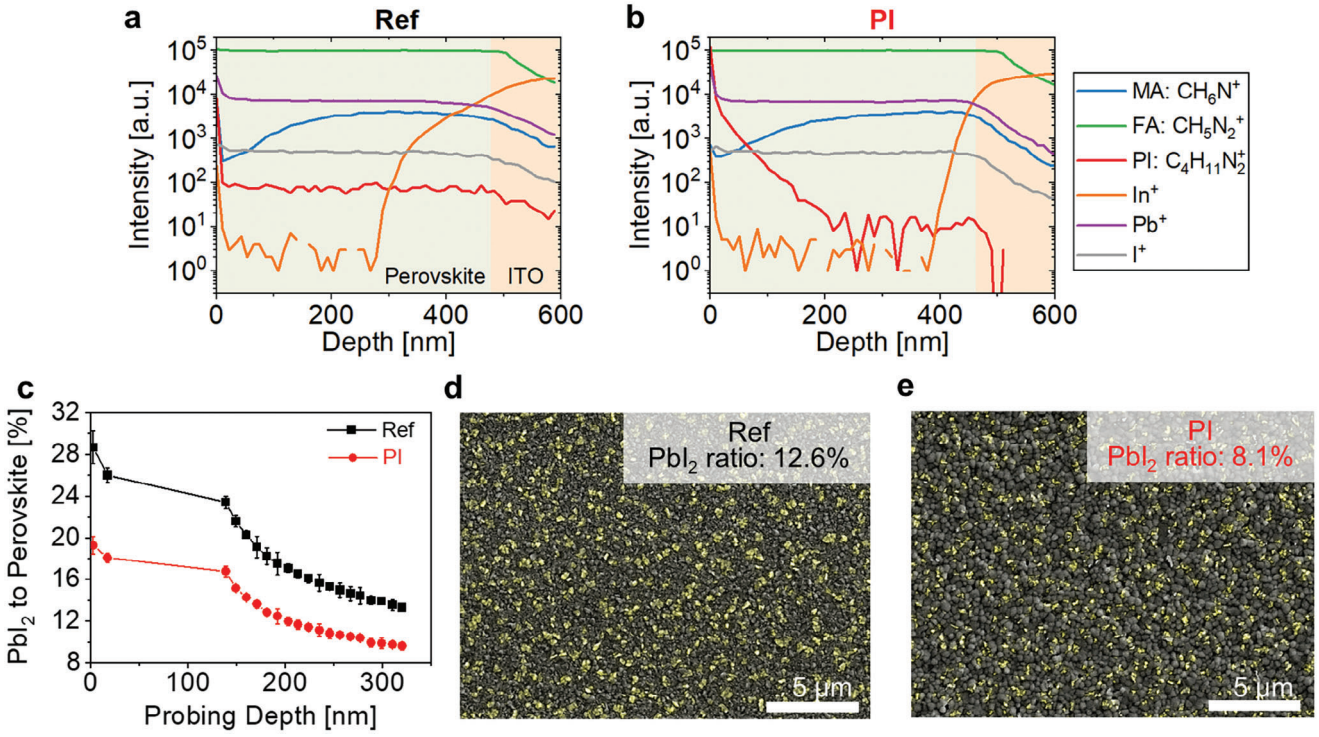

Figure 1. a,b) ToF-SIMS depth profile of reference and PI-treated perovskite films with the ionic traces of MA, FA, Pb, I, In, and piperazinium. Note, that the strong changes in signals at the near-surface region are due to surface artifacts inherent to SIMS data until surface contamination is removed and sputter equilibrium is achieved. Additional ionic traces determined from the TO-SIMS measurements are displayed in Figure S7 (Supporting Information). c) Peak area ratio of PbI_2 to perovskite (110) as a function of probing depth calculated from GIWAXS data at grazing angles ranging from 0° to 0.3°. d,e) Top-view SEM-CL images of the reference and PI-modified perovskites, respectively. The PbI_2 can be distinguished by overlaying the SEM secondary electron image (grey) with an SEM-CL intensity image (yellow).

to 2.0 mg mL^{-1}, were employed to determine the optimum conditions for the best performance, as detailed in Figures S4, S5 (Supporting Information). Solar cells employing 1 mg ml^{-1} PI showed the highest PCE, which can mostly be attributed to an increase. This suggests that, for multiple perovskite compositions, PI seems to be a very promising and unique molecule for surface treatment in high-efficiency top cells for tandem applications. In this study, we attempt to investigate the working mechanism of PI on the WBG perovskite and expand the understanding of its influence on structural properties, defect density, and charge carrier dynamics of the perovskite.

First, we investigated the influence of PI on the structural properties of the WBG perovskite. For this, we performed attenuated total reflection Fourier-transformed infrared (ATR-FTIR, Figure S6, Supporting Information) spectroscopy and time-of-flight secondary ion mass spectrometry (ToF-SIMS, **Figure 1**a,b) measurements to prove the existence of PI after treatment. Figure S6 (Supporting Information) displays the vibrational spectra of PI powder, perovskite, and PI-modified perovskite. The PI modification leads to a reduction of transmission in the fingerprint region (1050–1350 cm^{-1}), which is challenging to deconvolute, due to the multitude of different vibrational modes at low wavenumbers, which can also be observed in the spectrum of PI powder. Yet, no clear change in the amidic (N-H) vibration mode (≈3000–3500 cm^{-1})[59] could be observed, possibly due to the low concentration of PI and the occurrence of N-H bonds in the perovskite itself. These measurements indicate the presence of the piperazinium cation on the perovskite surface, without evidence of strong interaction with the organic framework of the perovskite. To further explore the integration of PI into the perovskite, ToF-SIMS measurements were performed. As expected, the ionized mass corresponding to piperazinium is in the noise level for the reference (Figure 1a), while for the PI-modified sample, the trace of a piperazinium cation expanding well into the perovskite was detected (Figure 1b). These results also demonstrate that the PI treatment does not alter the concentration of other constituents in the perovskite such as methylamine or formamidinium. A set of more device-relevant ionic species is displayed in Figure S7 (Supporting Information).

To understand the influence of PI on the WBG perovskite's crystal structure X-ray diffraction (XRD) in Bragg–Brentano and, grazing incidence (GIXRD, 0.2° GI angle) configuration, and grazing-incidence wide-angle X-ray scattering (GIWAXS) have been employed, with results shown in Figure 1c, Figures S8, S9 (Supporting Information). As seen in Figure S8a (Supporting Information), the crystal structure of perovskite films was not changed before and after PI modification. The GIXRD showed the changed diffraction intensity of PbI_2 at the surface of the PI-modified sample compared to the reference (Figure S8b, Supporting Information). To quantify the reduction of PbI_2, the GIWAXS measurements were employed by tuning the incidence angles between 0° and 0.3°, enabling us to collect signals from

various integrating depths in GIWAXS, as shown in Figure 1c. The PbI_2 content decreased from 28.7% to 19.3% on average after PI modification at the surface, which remains to influence the integrated signal over the whole considered probing depth.

The decrease of PbI_2 upon PI treatment and surface features of perovskite films were further confirmed by scanning electron microscopy cathodoluminescence (SEM-CL) with 500 nm CL emission and 500 ± 50 nm band pass filter, and SEM images. The PbI_2-to-perovskite coverage ratio reduced (i.e., 12.6% for the reference, and 8.1% for the PI-modified samples) upon PI modification, as evident from the overlay of the SEM secondary electron image (grey) with an SEM-CL intensity image (yellow), as shown in Figure 1d,e and Table S1 (Supporting Information). To exclude the solvent effect, we also conducted a control experiment, in which we rinsed the surface with IPA only. As expected, the SEM-CL analysis (Figure S10, Supporting Information) only shows a minor reduction of PbI_2 which is further confirmed by top-view and cross-sectional SEM images (Figure S11, Supporting Information). The role of surficial PbI_2 and its influence on optoelectronic properties was extensively investigated in previous studies and is still under debate.[60] Typically, it is found that an optimum surface coverage of PbI_2 enhances the device's performance.[55] Macroscopically, the PI treatment does not alter the optical properties of the perovskite absorber as evidenced by reflection and transmission measurements (Figure S12, Supporting Information).

Time-dependent steady-state PL spectra of the neat perovskite on quartz revealed that the PI-modified perovskite featured an improved photostability when compared with the reference sample (**Figure 2**a,b). The PI-modified sample showed a slight light soaking effect with increasing PL intensity over time, while it declined over time and suffered from the emergence of a second PL emission feature for the reference, possibly due to halide segregation.[10,61,62] To evaluate the initial non-radiative recombination losses, absolute PL measurements were conducted to determine the QFLS values (Figure S10b,c, Supporting Information). The QFLS constitutes the upper limit for the V_{OC} and can thus enable valuable insights into the optoelectronic quality of a photovoltaic absorber. The best QFLS of the PI-modified perovskite reached 1.45 eV and was therefore slightly higher than for the untreated reference (1.42 eV, see inset of Figure 2a,b). This indicates that the PI modification reduced the perovskite's non-radiative recombination losses, suggesting a passivation of the surface by, for example, a reduced defect density. This is different from our previous study, where even a decrease in QFLS after PI treatment of the absorber layer was found and hence no indication of a chemical passivation.[51] A detailed analysis of the influence of the charge transport materials (CTM) on QFLS follows below.

Transient PL (trPL) characterizations were conducted at one-sun equivalent charge carrier generation to evaluate the carrier lifetime (τ) and recombination losses, as shown in Figure 2c and Table S2 (Supporting Information). The carrier lifetime of the neat perovskite film on quartz improved significantly up to 3.32 µs after PI modification compared to 0.96 µs of the reference sample.

To further study the influence of the PI on the surface properties of the, we conducted near-UV photoelectron spectroscopy (PES) measurements with varying excitation energy in constant final state mode (CFSYS) for the perovskite with a layer stack of glass/ITO/2PACz/perovskite (without/with PI). Under the assumption of a constant dipole matrix element, CFSYS allows us to trace the density of occupied states over a large dynamic range in the valence band region and bandgap up to the Fermi edge.

The CFSYS spectra shown in Figure 2d are aligned at the modeled valence band maximum (VBM) to allow for a direct comparison of the density of occupied defects in units of the internal photoelectron yield.[63] The integrated density of defect states of the PI-modified perovskite was significantly decreased compared to the reference sample as indicated by the grey arrow in Figure 2d. This supports our results obtained by PL, suggesting chemical passivation as the origin of the increased charge carrier lifetime and enhanced QFLS of the PI-modified sample. Interestingly, a reduced defect density and increase in QFLS were not found for the PI-treated perovskite absorber in our above-mentioned study on a different perovskite composition.[51] The herein-found defect states are likely to be attributed to PbI_2 on the surface,[63] and their decrease is in line with the reduced PbI_2 concentration as discussed in the structural analysis above. Our results agree well with the chemical working mechanism of PI recently described by Li et al. as acting as both, an electron donor and acceptor while interacting with PbI_2 on the perovskite surface.[50]

Besides the influence of the defect density at the perovskite surface, also the energy level alignment with the CTMs can play a crucial role in the device's performance. The energetic positions of the VBM and work function (WF) with respect to the surface Fermi level (E_F*) were determined from the CFSYS and UPS ($h\nu$ = 6.5 eV) spectra as shown in Figure S14 (Supporting Information) and summarized in Figure 2e according to our previously established fitting procedure.[64] We found that the Fermi-level of the PI-modified sample shifted slightly further away from the VBM as compared to the reference: $E_V - E_F$* increased from −1.45 to −1.55 eV. Considering the optical bandgap of the perovskite (1.8 eV), the conduction band minimum (CBM) of the reference and PI-modified perovskites was determined to 0.35 and 0.25 eV above the Fermi-level, respectively, indicating an increased electron concentration at the perovskite surface after PI treatment. The WF of the reference and PI-modified samples is found to be very similar with 4.45 and 4.48 eV (Figure S14c, Supporting Information), respectively. Hence, the ionization energy of the PI-modified perovskite was increased by ≈130 meV compared to the reference, which might be due to the formation of a positive dipole on the surface. A downward offset between the perovskite conduction band minimum and the C_{60} LUMO can be reduced by such a dipole and thereby lead to a beneficial energy level alignment.[51,64]

The dipole obtained here is roughly half the size of the dipole found in our previous study, which might be caused by the different perovskite composition and/or PI concentration. To fully reveal the chemical and physical mechanisms, a broader survey study is required. Here, our results suggest that both the dipole and decrease in surface defects contribute to the improved interface.

To gain more insight into the defect physics, we applied a unique version of four-point probe photo-Hall measurements, based on a combination of light illumination with magnetic field: CLIMAT (Figure S15a,b, Supporting Information, see the Experimental Section, Supporting Information for more details).[52,53]

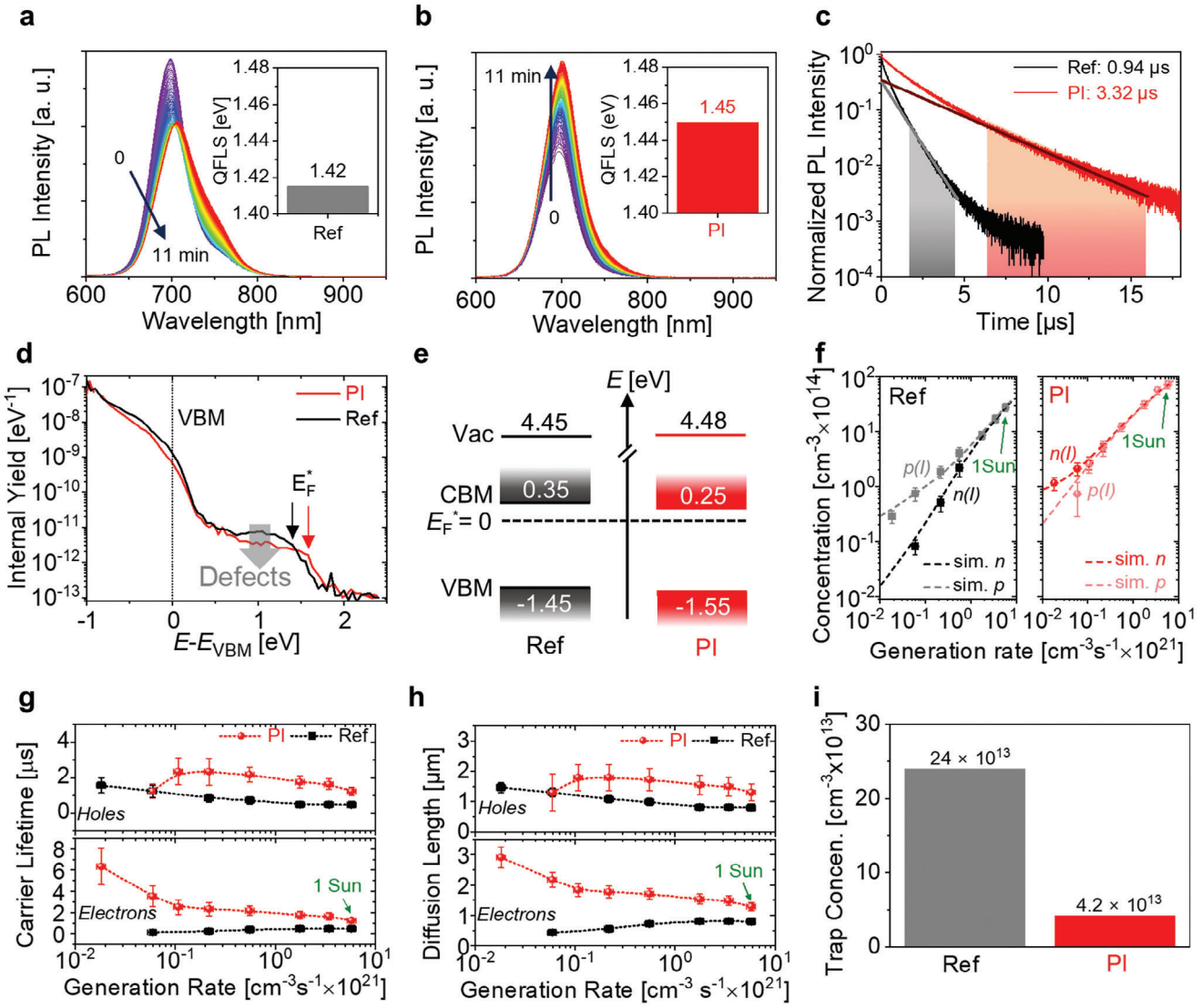

Figure 2. a,b) Steady-state PL spectra recorded as a function of time (11 min duration) for reference and PI-modified perovskites on a quartz substrate. The inset shows the initial QFLS of the reference and PI-modified perovskites. c) PL transients of the reference and PI-modified perovskites on quartz substrates. The noted lifetimes assigned to radiative recombination in the perovskite are fitted with an exponential function over the ranges marked in light red and grey. d) Valence band spectra measured by constant final state yield spectroscopy (CFSYS) of the perovskite with and without PI modification. The spectra are aligned to the modeled VBM and the Fermi level at the surface (E_F^*) is indicated by small black and red arrows. The grey arrow indicates the reduced density of defect states within the bandgap. e) Energetic positions of the perovskites' valence and conduction band edges as well as the vacuum level determined by near-UV PES. f) Electron *n(I)* and hole *p(I)* concentrations as a function of the generation rate (*I*) as extracted from CLIMAT measurements. The simulated concentrations are included as dashed lines and measured data as symbols. g,h) Carrier lifetime and diffusion length of the reference and PI-modified perovskites calculated from the concentration of electrons and holes under various illumination intensities. The marked "1 sun" values correspond to a photogeneration equal to standard test conditions (AM1.5G spectrum, irradiance 100 mW cm^{-2}). i) Deep trap concentrations of the reference (Ref.) and PI-modified perovskites as simulated from the CLIMAT results.

This method allows to disentangle concentrations, lifetimes, and diffusion lengths of electrons and holes and ultimately determines the bulk defect density by probing charge transport in the plane parallel to the substrate. Illumination parameters in a steady-state regime closely resembling "one sun" conditions, reveal charge carrier transport that is essential to solar cell operation conditions.

First, we investigate the conductivity, Hall coefficient, and Hall mobility under various steady-state illumination conditions (Figure S15d,e, Supporting Information), which can be extracted by measuring the longitudinal voltage induced by the electrical current without applied magnetic field and transverse Hall voltage under oscillating the magnetic field. With this, the electron and hole concentration (n and p), mobilities (μ_e and μ_h), lifetimes (τ_e and τ_h), and diffusion lengths (L_e and L_h) can be determined. The reference sample showed a significant p-type conductivity for low generation rates, whereas the PI-modified sample exhibited n-type conductivity (Figure 2f; Figure S15f, Supporting

Information). This trend toward higher electron concentration for PI-modified layers is consistent with the Fermi level approaching the CBM as observed by CFSYS. Note, that the absolute values are however very different, which is reasonable to be expected. We attribute this to first, the different probing atmospheres and second, the different probing depths of the measurement techniques. The probing atmosphere has been found to strongly impact the sample work function with typically much lower work function under UHV conditions for PES as compared to ambient or inert atmosphere (for CLIMAT).[65] Furthermore, PES measurements are highly surface sensitive and only probe the topmost few nm, while CLIMAT measurements are bulk sensitive and hence over all much less sensitive to surface defects or band bending. As the reference and PI-modified perovskites are *p*- or *n*-type, respectively, the free hole (μ_h) and electron (μ_e) mobilities (0.53 and 0.55 $cm^2\ V^{-1}\ s^{-1}$) can be directly assigned to the dominant carrier type at low illumination conditions (see Equation SH3, Figure S15d,f, Supporting Information). With increased illumination, the Hall mobility decreased to the difference of electron and hole mobilities, as predicted by Equation SH3 (Supporting Information). Note that Hall mobility includes the contribution of both free electrons and holes ($\mu_p^2 p$ and $\mu_e^2 n$ in Equation SH3, Supporting Information) and thus can decrease when μ_h and μ_e become similar.

Electron and hole concentrations (*n* and *p*) can be calculated by solving the equations for semiconductor conductivity (Equation SH1, Supporting Information) and for the Hall coefficient (Equation SH2, Supporting Information) with mobilities found in the low illumination regime. The charge carrier lifetimes and diffusion lengths as functions of the generation rate were calculated according to Equations SH4–SH7 (Supporting Information) and are visualized in Figure 2g,h. The lifetimes of electron and hole become similar as the illumination intensity is increased while they are distinctly different at low and moderate illumination conditions, as shown in Figure S15g,h (Supporting Information). To the best of our knowledge, such a difference between hole and electron lifetimes was not revealed previously by other methods due to natural limitations (e.g., in photoluminescence and photoconductivity transient methods only one type of carrier is detected) or unjustified simplifications ($\tau_e = \tau_h$).[66–68]

For device-relevant illumination conditions, one sun intensity was considered. Since high injection conditions are reached at this intensity, both densities and lifetimes of electrons and holes become equal. For the PI-modified sample, the charge carrier lifetimes, and consequently the diffusion lengths of holes and electrons significantly increased compared to the reference (Figure 2g,h). The charge carrier lifetime was increased from 0.48 to 1.24 µs and the diffusion length from 0.81 to 1.30 µm (Table S3, Supporting Information). These lifetimes show the same trend as determined by trPL but are slightly lower in absolute numbers, which might be due to different measurement conditions (steady-state vs pulsed illumination). To the best of our knowledge, these steady-state diffusion lengths of the electrons and holes are among the longest values compared with previous reports on polycrystalline metal-halide perovskites.[66–68]

The knowledge of hole and electron concentration as a function of intensity allows us to develop charge transport simulations (more details in Note II, Supporting Information) with the theoretical model considering non-radiative and radiative recombination. Performing our simulations in a steady-state condition allows us to further understand the charge losses (more details in Note II, Supporting Information). For reproducing the experimental CLIMAT data, different models with various trap state characteristics (deep vs shallow) were tested. Only the model with deep trap states could explain the measured data for the transport of electrons and holes (Table S4, Supporting Information), hence they dominate the charge recombination processes. By this modeling, we find that the deep trap concentration is reduced from 24×10^{13} cm^{-3} to 4.2×10^{13} cm^{-3} by the PI treatment (Figure 2i; Figure S15g,h, Table S4, Supporting Information). The observed decrease of deep trap concentration is consistent with the ToF-SIMS results above, which proved the penetration of the piperazinium cation well into the bulk and can thereby chemically passivate the perovskite.

Next, we study the photovoltaic performance of single-junction WBG solar cells with a layer stack of glass/ITO/2PACz/WBG perovskite/C_{60}/SnO_2/Cu (**Figure 3a**). Prior to the analysis of full solar cells, we performed a layer-by-layer loss analysis with absolute PL measurements adding none, one, or both CTMs but leaving out the SnO_2 buffer layer and Cu electrode. The calculated QFLS values (Figure 3b) show that the neat perovskite reached 1.45 eV after PI modification with 2.2% PL quantum yield (Figure S17, Supporting Information), which marked an improvement over the reference sample (1.42 eV). When only adding C_{60} on top of the perovskite, the QFLS of the reference sample was strongly reduced to 1.37 eV, while the PI-treated sample retained its high QFLS of 1.45 eV. This indicates that the PI modification successfully inhibited non-radiative recombination losses that occurred at the perovskite/C_{60} interface. Upon the addition of 2PACz, the QFLS of the reference and PI-modified samples were only slightly reduced, which indicated low recombination losses at that interface.[4,9] When combined with both, 2PACz and C_{60}, the PI-modified perovskite achieved a QFLS of 1.42 eV as compared to 1.32 eV for the reference (Figure 3b; Figures S13, S17, Supporting Information).

Analogous to the analysis of the absolute PL, we studied the recombination of charge carriers with transient PL (Figure S18a–c, Supporting Information) and computed differential lifetimes to separate the charge transfer process from trap-assisted recombination,[69] as shown in Figure S18d–f (Supporting Information). After depositing C_{60}, trPL transients indicated a much longer decay time for the PI-modified perovskite compared to the reference sample on quartz substrates (8.78 µs vs 0.89 µs, Figure S18a, Table S2, Supporting Information). Furthermore, on a glass/ITO/2PACz substrate, the PI-modified perovskite also had a longer trPL transient compared to the reference sample, as shown in Figure S18b (Supporting Information). In the complete layer stack (glass/ITO/2PACz/perovskite/C_{60}), the trPL transients of the PI-modified perovskite, yield a remarkable mono-exponential decay lifetime >10 µs compared to <1 µs for the reference sample, as shown in Figure S18c (Supporting Information). These remarkable improvements in the trPL decay lifetime of the PI-modified perovskites, both with and without C_{60} can be attributed to the significant reduction of the non-radiative recombination losses and likely to the reduction of trap states. This analysis revealed a significantly improved interface between

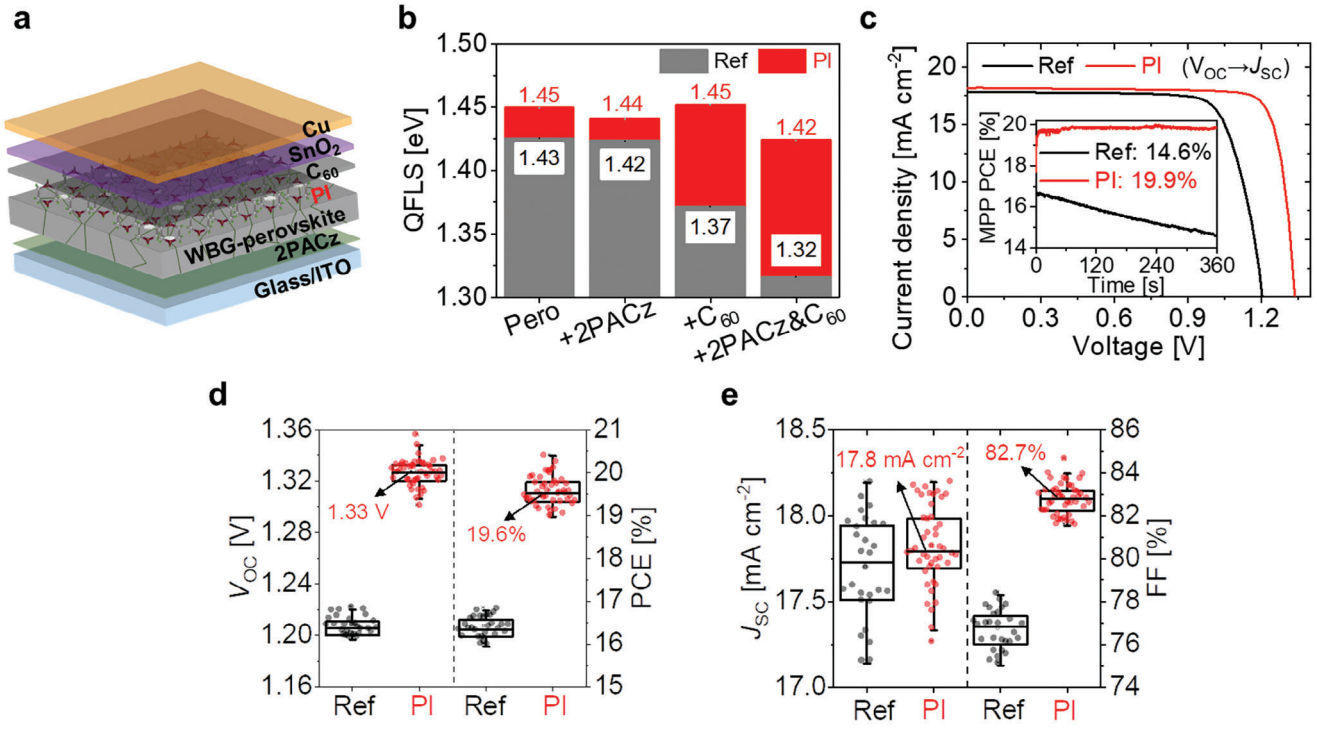

Figure 3. a) Schematic stack of the WBG PSC. b) Layer-by-layer analysis of WBG perovskite QFLS with and without PI modification in the following layer stacks quartz/perovskite, glass/ITO/2PACz/perovskite, quartz/perovskite/C_{60}, glass/ITO/2PACz/perovskite/C_{60}. c) Reverse scan *J–V* curves of the best reference and PI-modified PSCs, measured with an aperture of 0.12 cm^2. The corresponding *J–V* parameters are displayed in Table 1. Inset: PCE during 6 min MPP tracking. d,e) Statistic performance of reference (26 devices) and PI-modified PSCs (28 devices) under illumination. The average *J–V* parameters of PI PSCs are presented in the figures. The middle horizontal line of the boxes represents the mean value, and the boxes span over the standard deviation.

the perovskite and CTMs with PI modification by reducing non-radiative recombination losses.

Subsequently, we carried out *J–V* measurements to determine the photovoltaic performance. Figure 3c displays *J–V* characteristics of the best PI-modified and reference device. The PV performance parameters of PSCs with and without PI modification were characterized and are shown in Figure 3d,e and **Table 1**. The best PI-modified PSC achieved a V_{OC} of 1.34 V, an FF of 83.9%, and a PCE of 20.3%, which is a clear improvement over the reference device (V_{OC}: 1.20 V, FF: 77.6%, PCE:16.6%). To the best of our knowledge, this result marks one of the first PSC with a bandgap of ≈1.8 eV surpassing a PCE of 20%.[34,35,40,45,47,70,71] The photogenerated current densities (J_{ph}) calculated from external quantum efficiency (EQE) spectra (Figure S19a, Supporting Information) agree well with the J_{SC}s determined from *J–V* characterization.

The MPP tracking (inset of Figure 3c) demonstrates that the PI modification strongly improved the steady-state operational stability of the PSC. This is in line with the improved photostability discussed above and the suppression of degradation in grain morphology as evidenced by SEM images before and after annealing (Figure S20, Supporting Information). In addition, the PSCs stability was also improved in longer MPP tracking and shelf-storage in the glovebox (Figure S19b,c, Supporting Information). The PI-modified PSCs exhibited a significantly improved performance compared to reference samples, with mean values of 1.33 V (V_{OC}), 82.7 % (FF), 19.6% (PCE), and 17.8 mA cm^{-2} (J_{SC}), respectively (Figure 3d,e). Remarkably, the maximum V_{OC} with PI-modified PSC reached 1.36 V with a 20.0% PCE (Figure S19d, Supporting Information). This marks an $E_g/q - V_{OC}$ deficit of only 0.44 V, which marks the highest PCE at a bandgap of 1.80 eV and the highest V_{OC} achieved for a PSC with a bandgap <1.85 eV (Figure S19e,f, Supporting Information).[10,15,21,34,35,54,72,73] The

Table 1. Photovoltaic performance parameters of the best WBG and NBG single-junction PSCs, and APTSCs. The measurement apertures of champion WBG- and NBG-PSCs, and APTSCs are 0.12, 0.10, and 0.12 cm^2, respectively. Reverse (forward) scan direction refers to scanning from open-circuit to short-circuit conditions (or vice versa).

Sample	Scan direction	V_{OC} [V]	J_{SC} [mA cm^{-2}]	FF [%]	PCE [%]	MPP PCE [%]
WBG Ref	Reverse	1.20	17.8	77.6	16.6	14.6
	Forward	1.19	17.8	77.1	16.4	
WBG PI	Reverse	1.34	18.2	83.9	20.3	19.9
	Forward	1.33	18.2	81.3	19.6	
NBG Ref	Reverse	0.78	31.5	74.2	18.3	16.3
	Forward	0.77	31.4	70.2	17.0	
NBG RbI	Reverse	0.85	31.4	76.7	20.6	18.8
	Forward	0.84	31.4	73.2	19.3	
Certified Tandem	Reverse	2.113	16.0	81.4	27.4	27.2
	Forward	2.111	16.1	80.9	27.5	

QFLS still surpasses the best V_{OC}, of which the possible reason will be discussed below.

Additionally, light-intensity-dependent *J*–*V* curves reveal a reduction of the ideality factor from 1.48 to 1.35 after PI modification (Figure S21, Supporting Information), which is indicative of reduced non-radiative recombination and thus in good agreement with the findings presented above. To further evaluate the performance potential of the WBG perovskite, a layer-by-layer analysis analogous to the results above (Figure 3b) was performed by means of intensity-dependent absolute PL measurements (Figure S22, Table S5, Supporting Information). With the PI-modification, the drop of the pseudo-FF (pFF) invoked by the CTMs is less (from 88.1 to 87.4%) than for the reference sample (88.4% to 86.4%). As a result of the improved pV_{OC} and pFF, the pseudo-PCE (pPCE) of the PI-modified sample reached 21.8% as compared to 19.4% for the reference device (assuming a J_{SC} of 17.8 mA cm^{-2} from the EQE optimized device as above). In view of previous studies on different compositions[50,51] our results demonstrate that the PI treatment can enhance the V_{OC} for a wide range of triple halide perovskite compositions.

2.2. Tandem Integration

To realize all-perovskite tandems, a bottom cell with an NBG tin-lead (Sn-Pb) perovskite was developed. For this, the performance of an NBG perovskite with the composition $Cs_{0.1}FA_{0.6}MA_{0.3}Pb_{0.5}Sn_{0.5}I_3$[43] was optimized with rubidium iodide (RbI) additive according to our previous report for a different composition.[74] The details of the optimization process and solar cell results are described in Note III, Figures S23–S26, and Table S6 (Supporting Information). The RbI-optimized NBG solar cells achieved a V_{OC} of 0.85 V, which resulted in an improved PCE of 20.6% (reference: 18.3%), as shown in Table 1 and Figure S26b (Supporting Information). This demonstrates that RbI is an efficient additive for various NBG perovskite compositions for bottom-cell utilization.

We combined the optimized WBG and NBG single junctions into APTSC. The schematic layout of the monolithic tandem cell is displayed in **Figure** 4a. The tandem cell consists of the optimized WBG top cell with PI modification, which was electrically coupled to the optimized NBG bottom cell with RbI additive through a 100 nm thick ITO recombination contact, which protects the WBG subcell from damage during fabrication of the NBG subcell and reduces reflection losses (see Figure S27, Supporting Information). To improve the optical performance of the device, an anti-reflection foil was glued to the substrate glass. A detailed optical analysis is shown in Note IV, Figures S28, S29 and Table S7 (Supporting Information). The cross-sectional morphology of the tandem device in Figure 4b shows layer thicknesses of ≈400 nm (WBG) and ≈1000 nm (NBG), respectively, both demonstrating good crystallinity in the final tandem stack.

Figure 4c displays the *J*–*V* curves and 5 min MPP tracking (inset figure) of a tandem cell that was certified at the Japan Electrical Safety & Environmental Technology Laboratories (JET, the full set of certification measurements is displayed in Figure S30, Supporting Information). The certified cell exhibits a V_{OC} of 2.11 V (2.11 V), an FF of 80.9% (81.4%), and a PCE of 27.5% (27.4%) in the forward (reverse) scan. The certified device sustained a PCE of 27.2% over 5 min MPP tracking. The certified values for the integrated photogenerated current density for the top and bottom subcell ($J_{ph,\,WBG}$, and $J_{ph,\,NBG}$) reached 16.2 and 16.1 mA cm^{-2}, which are consistent with integrated values extracted from EQE spectra measured in-house, as shown in Figure 4d. The tandem cell exhibited a low current loss in the top cell, while the bottom cell still suffered from relatively high internal and reflection losses due to the lower absorption coefficients in the band-edge region as compared to Pb-based perovskites (for a summary of optical losses, refer to Table S7, Supporting Information).[13,75] The thickness of our NBG perovskite layer is limiting the absorption of infrared photons compared with a previous report.[27] The PV parameters of this certified tandem sample were also measured in-house before certification (see Figure S31a,b, Supporting Information), and agree well with the certified values. The best V_{OC} of all fabricated tandem devices was measured to be >2.15 V with a negligible hysteresis, as shown in Figure S27c and Table S8 (Supporting Information). This tandem V_{OC} value is better or comparable to values reported for the best APTSCs.[14–16,20,22,27,28,34,35,42,58,76] The statistical distribution of the performance parameters is displayed in Figure 4e and Figure S31d–f (Supporting Information). They show a narrow distribution with an average V_{OC} of 2.11 ± 0.02 V and PCE of 27.2%. To evaluate the stability of our tandem cells, a long-term MPP track under atmospheric conditions and room temperature was performed after encapsulation (Figure 4f). The tandem device showed a rise in efficiency during the first 50 h, which is in line with the PL results also showing enhanced emission over time (Figure 2b). After 264 h of MPP tracking, the tandem sustained 88.5% of its initial PCE, which is comparable to the stability reported for an APTSC with a similar PCE.[30]

To further study the efficiency potential of our tandem cells, pseudo *J*–*V* curves were acquired from illumination-intensity dependent *J*–*V* measurements,[55] absolute-injection dependent electroluminescence (EL),[4,5,58,77–79] and absolute-intensity-dependent PL.[58,77,78] For this purpose, a structurally identical tandem cell with a PCE of 27.5%, (performance parameters in Table S9) was used. As shown in Figure 4g and Table S9 (Supporting Information), the pseudo *J*–*V* parameters of this cell achieved a pFF of 83.4% and 28.7% pPCE (assuming J_{SC} of 16.3 mA cm^{-2}) when extracting values from intensity-dependent *J*–*V* curves (suns-V_{OC}), which agrees well with the pseudo *J*–*V* generated by EL (inset table of Figure 4g). A pV_{OC} of 0.815 V for the NBG subcell was lower than expected from the single-junction *J*–*V* characterization, which could be due to the adapted annealing temperature of PEDOT: PSS in the tandem application to reduce the thermal load for the WBG perovskite (120 °C for 10 min vs 150 °C for 20 min). Interestingly, the pV_{OC} of the NBG perovskite determined from absolute PL measurements was 52 mV higher than that obtained from EL. According to previous reports, this significant discrepancy could be evoked by an energetic mismatch in the band structure of perovskite and CTMs[58,78] or more generally due to a poor selectivity of a CTM (i.e., a low majority/minority carrier conductivity ratio next to the limiting interface).[80] In contrast, the pV_{OC} of the WBG from PL was 1.31 V and thus only slightly higher than the 1.29 V determined from EL. As a result, the pV_{OC} of the tandem device extracted from PL achieved 2.18 V with a pseudo PCE of 30.4%,

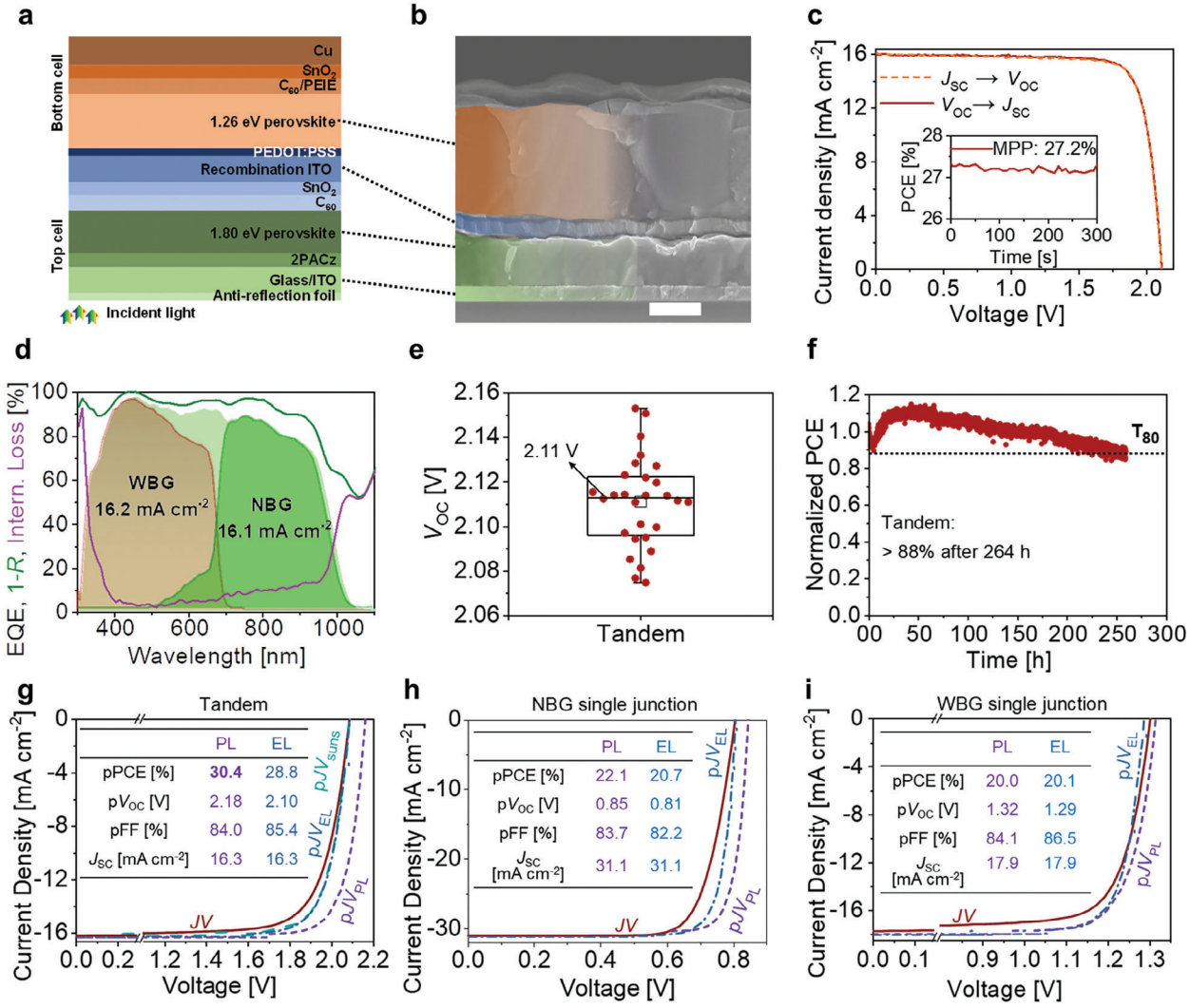

Figure 4. a) Sketch of the all-perovskite tandem solar cell stack. b) Cross-sectional SEM image of the tandem solar cell. The scale bar is 400 nm. c) *J–V* curves, and 5 min MPP tracking (inset) of the certified tandem solar cell. The aperture for the certification measurement is 0.1212 cm^2. d) EQE spectra of the certified tandem solar cell, including the 1-reflection (1-*R*), internal optical losses, and the cumulated EQE of the two subcells (light green). e) Statistical V_{OC} distribution of 28 tandem cells. The measurement aperture is 0.1225 cm^2. The middle horizontal line of the boxes represents the mean value, and the boxes span over the standard deviation. f) Long-term MPP stability of an encapsulated all-perovskite tandem solar cell recorded in ambient air at 25 °C, with no humidity control. The initial efficiency was 26.8% from *J–V* scans. The 80% (T_{80}) of peak efficiency of tandem solar cells is included according to the ISOS standards. g–i) *J–V* and pseudo *J–V* (pJV_{suns}, only in g) curves of the tandem, NBG, and WBG solar cell calculated from intensity-dependent sun simulator measurements, as well as pseudo *J–V* curves calculated from intensity-dependent EL (pJV_{EL}) and PL (pJV_{PL}) measurements on the same sample.

which sets a realistic limit, if the series resistance losses could be further reduced. To understand the losses in more detail, the single-junction *J–V* and pseudo *J–V* curves (PL and EL) of the NBG and WBG PSCs were also measured (Figure 4h,i). Similar to the results obtained for the tandem cell, also the characterization of the subcells shows lower pV_{OC}s from EL than PL (NBG: 40 mV, WBG: 30 mV; see inset tables of Figure 4h,i). We thus conclude that for further improvements of the performance, it is necessary to develop new HTMs with better energetic alignment to the NBG perovskite. Overall, the results from the pseudo *J–V* measurements highlight that the PCE of the all-perovskite tandem solar cells could surpass 30%. In addition, improvements in the thermal stability are another key to further increase the V_{OC} of the WBG PSCs (see Note V and Figure S32, Supporting Information) and enable >30% efficient all-perovskite tandem solar cells.

3. Conclusion

We developed a new triple-halide perovskite with a bandgap of 1.80 eV and implemented a piperazinium iodide (PI) surface treatment, which virtually eliminated all non-radiative recombination losses at the perovskite/C_{60} interface. This study for the first time demonstrates the successful application of PI to WBG triple-halide perovskite absorbers and thereby shows the versatility of PI to improve the interface properties of different metal-

halide perovskites. Moreover, this study combines detailed structural analysis with optoelectronic investigations and modeling to further understand the influence of PI on device performance. The structural analysis with ATR-FTIR and ToF-SIMS proved the presence of PI at the surface and its penetration into the bulk. Furthermore, XRD measurements demonstrated that the PI modification decreases the PbI_2 fraction at the surface. Subsequently, near-UV PES measurements with varying excitation energy in constant final state mode (CFSYS) were employed to characterize the surface energetics. Here, we found that both chemical passivation by the decrease of surface and bulk defect states and an electrostatic dipole contribute to reduced non-radiative recombination and potentially improved energy level alignment to the ETM, which is distinctively different from earlier studies. Moreover, we use CLIMAT measurements to further understand the PI's effect on charge transport by separately resolving and quantifying electron and hole charge transport properties under varying illumination conditions. These measurements revealed that the PI modification significantly increased the steady-state carrier lifetime and diffusion length compared to the reference samples. We devised a model to simulate charge transport, which suggested that the PI treatment decreases the defect concentration and thus leads to better charge transport and a boost in PCE. A record V_{OC} of 1.36 V of WBG-PSCs was achieved with 20% PCE after PI modification. Combining this superior WBG-PSCs with a narrow bandgap perovskite for monolithic all-perovskite tandems, we achieved certified PCEs of 27.5% and 27.2% from *J–V* scans and MPP tracking, respectively. Encapsulated tandem cells sustained >88% of the initial efficiency after 264 h of continuous MPP tracking in air. To estimate the PCE potential, intensity-dependent absolute photoluminescence measurements were performed and demonstrated that our tandem design can potentially achieve >30% PCE. Overall, our study provides important scientific insights to accelerate the development toward commercialization of this technology.

Supporting Information

Supporting Information is available from the Wiley Online Library or from the author.

Acknowledgements

The authors are grateful to C. Ferber, T. Lußky, H. Heinz, and J. Beckedahl for daily technical assistance in the laboratory, C. Klimm for SEM support, and M. Härtel for help with optimizing the TCO sputtering. The authors further thank E. Neumann and P. Husemann (Department of Chemistry, TU Berlin, Germany) for ATR-FTIR measurements. The authors acknowledge funding from the Deutsche Forschungsgemeinschaft (DFG, German Research Foundation) within the SPP 2196 (HIPSTER-PRO 424709669). M.S. further acknowledges the Heisenberg program from the Deutsche Forschungsgemeinschaft (DFG, German Research Foundation) as well as the Vice Chancellor Early Career Professorship Scheme from CUHK for funding, Project No. 498155101. This work was partly funded by EPSRC, project number EP/S004947/1. Funding was provided by the Federal Ministry of Education and Research (BMBF) through Young Investigator Group Perovskite Tandem Solar Cells within the program "Materialforschung für die Energiewende" (grant no. 03SF0540) as well as the project PEROWIN (grant no. 03SF0631) and by the Helmholtz Association within the projects HySPRINT Innovation lab, the EU Partnering project TAPAS and the project "Zeitenwende – Tandem Solarzellen". A.M. and F.S. acknowledge financial support from the German Science Foundation (DFG) in the framework of the priority program SPP 2196 and funding from the European Union HORIZON-MSCA-2021-PF-01-01 under grant agreement no. 101061809 (HyPerGreen). A.M. gratefully acknowledges Danny Kojda and Klaus Habicht for their assistance with the Hall setup. The authors further acknowledge HyPerCells, a joint graduate school of the University of Potsdam and the Helmholtz-Zentrum Berlin. The authors gratefully acknowledge DESY, Hamburg for the granting of beamtime and support by the beamline staff of beamline P08, especially F. Bertram. F.L. acknowledges funding from the Volkswagen Foundation via the Freigeist Program. K.B. and T.R. acknowledge funding by HIPSTER PRO (DFG, SPP2196, RI 1551/15-2), and MUJUPO^2 (DFG, RI 1551/12-2). The research leading to these results had received partial funding from the European Union's Horizon 2020 Programme under grant agreement no. 951774 (FOXES). This work was authored in part by the National Renewable Energy Laboratory, operated by Alliance for Sustainable Energy, LCC, for the U. S. Department of Energy (DOE) under contract no. DE-AC3608GO28308. We acknowledge the support on perovskite films' preparation from the Advanced Perovskite Cells and Modules program, and the support on ToF-SIMS analysis from the Hybrid Tandem Core program of the National Center for Photovoltaics, funded by the U. S. Department of Energy Office of Energy Efficiency and Renewable Energy, Solar Energy Technologies Office. The views expressed in the article do not necessarily represent the views of the DOE or the U. S. Government.

Open access funding enabled and organized by Projekt DEAL.

Conflict of Interest

The authors declare no conflict of interest.

Author contributions

F.Y. and S.A. coordinated the project and designed the experiments. F.Y., S.A., and P.T. co-designed the all-perovskite tandem solar cells and their characterizations. F.Y. executed experiments of samples' preparation and protocol modification and conducted the characterizations of the XRD, PL, trPL, solar cells, and the data analysis with the help of S.A., P.T., E.K., S.M., K.X., A.A., R.M., and L.K.P.T. conducted ideality factor measurement for the WBG PSCs and supported EQE measurement for tandem solar cells. A.M. designed and built the CLIMAT setup and method, conducted the CLIMAT study, results analysis, model design, and simulation of charge transport. D.M. contributed to the PES characterization and analysis. F.L. and M.S. conducted the PL and EL measurements of tandem devices. R.M. supported trPL measurement and setup modification. E.K. conducted sun simulator intensity-dependent measurements for pseudo *J–V* curves. K.X. introduced the 1.68 eV bandgap perovskite. S.H. performed ToF-SIMS measurements. S.M. introduced the PI processes. D.M. synthesized the PI ionic liquid molecules. L.M., A.H., and F.S. carried out the GIWAXS characterization and analysis. J.Z. conducted the power dependence PL of perovskite films for p*JV*. B.L. conducted the stability evaluation of tandem solar cells. F.S. supported the PI optimization. M.R. supported the evaluation of ATR-FTIR measurements. S.B. prepared additional samples for ATR-FTIR measurements. J.T. supported the discussion of NBG perovskite. F.Y., P.T., A.M., D.M., L.K., and S.A. created and designed the initial manuscript. All authors contributed to the data discussion, manuscript writing, and revision. S.A. supervised this project.

Data Availability Statement

The data that support the findings of this study are available from the corresponding author upon reasonable request.

Keywords

all-perovskite tandem solar cells, piperazinium iodide, recombination losses, triple-halide wide-bandgap perovskite

Received: August 2, 2023
Revised: November 6, 2023
Published online: December 6, 2023

[1] W. Liao, D. Zhao, Y. Yu, N. Shrestha, K. Ghimire, C. R. Grice, C. Wang, Y. Xiao, A. J. Cimaroli, R. J. Ellingson, N. J. Podraza, K. Zhu, R. G. Xiong, Y. Yan, *J. Am. Chem. Soc.* **2016**, *138*, 12360.
[2] T. Leijtens, K. A. Bush, R. Prasanna, M. D. McGehee, *Nat. Energy* **2018**, *3*, 828.
[3] R. Wang, T. Huang, J. Xue, J. Tong, K. Zhu, Y. Yang, *Nat. Photonics* **2021**, *15*, 411.
[4] A. Al-Ashouri, E. Köhnen, B. Li, A. Magomedov, H. Hempel, P. Caprioglio, J. A. Márquez, A. B. M. Vilches, E. Kasparavicius, J. A. Smith, N. Phung, D. Menzel, M. Grischek, L. Kegelmann, D. Skroblin, C. Gollwitzer, T. Malinauskas, M. Jošt, G. Matič, B. Rech, R. Schlatmann, M. Topič, L. Korte, A. Abate, B. Stannowski, D. Neher, M. Stolterfoht, T. Unold, V. Getautis, S. Albrecht, *Science* **2020**, *370*, 1300.
[5] J. Liu, M. De Bastiani, E. Aydin, G. T. Harrison, Y. Gao, R. R. Pradhan, M. K. Eswaran, M. Mandal, W. Yan, A. Seitkhan, M. Babics, A. S. Subbiah, E. Ugur, F. Xu, L. Xu, M. Wang, A. ur Rehman, A. Razzaq, J. Kang, R. Azmi, A. A. Said, F. H. Isikgor, T. G. Allen, D. Andrienko, U. Schwingenschlögl, F. Laquai, S. De Wolf, *Science* **2022**, *377*, 302.
[6] D. Kim, H. J. Jung, I. J. Park, B. W. Larson, S. P. Dunfield, C. Xiao, J. Kim, J. Tong, P. Boonmongkolras, S. G. Ji, F. Zhang, S. R. Pae, M. Kim, S. B. Kang, V. Dravid, J. J. Berry, J. Y. Kim, K. Zhu, D. H. Kim, B. Shin, *Science* **2020**, *3433*, eaba3433.
[7] Q. Han, Y. T. Hsieh, L. Meng, J. L. Wu, P. Sun, E. P. Yao, S. Y. Chang, S. H. Bae, T. Kato, V. Bermudez, Y. Yang, *Science* **2018**, *361*, 904.
[8] H. Shen, T. Duong, J. Peng, D. Jacobs, N. Wu, J. Gong, Y. Wu, S. K. Karuturi, X. Fu, K. Weber, X. Xiao, T. White, K. Catchpole, *Energy Environ. Sci.* **2018**, *11*, 394.
[9] A. Al-Ashouri, A. Magomedov, M. Roß, M. Jošt, M. Talaikis, G. Chistiakova, T. Bertram, J. A. Márquez, E. Köhnen, E. Kasparavičius, S. Levcenco, L. Gil-Escrig, C. J. Hages, R. Schlatmann, B. Rech, T. Malinauskas, T. Unold, C. A. Kaufmann, L. Korte, G. Niaura, V. Getautis, S. Albrecht, *Energy Environ. Sci.* **2019**, *12*, 3356.
[10] K. O. Brinkmann, T. Becker, F. Zimmermann, C. Kreusel, T. Gahlmann, M. Theisen, T. Haeger, S. Olthof, C. Tückmantel, M. Günster, T. Maschwitz, F. Göbelsmann, C. Koch, D. Hertel, P. Caprioglio, F. Peña-Camargo, L. Perdigón-Toro, A. Al-Ashouri, L. Merten, A. Hinderhofer, L. Gomell, S. Zhang, F. Schreiber, S. Albrecht, K. Meerholz, D. Neher, M. Stolterfoht, T. Riedl, *Nature* **2022**, *604*, 280.
[11] W. Chen, Y. Zhu, J. Xiu, G. Chen, H. Liang, S. Liu, H. Xue, E. Birgersson, J. W. Ho, X. Qin, J. Lin, R. Ma, T. Liu, Y. He, A. M. C. Ng, X. Guo, Z. He, H. Yan, A. B. Djurišić, Y. Hou, *Nat. Energy* **2022**, *7*, 229.
[12] X. Chen, Z. Jia, Z. Chen, T. Jiang, L. Bai, F. Tao, J. Chen, X. Chen, T. Liu, X. Xu, C. Yang, W. Shen, W. E. I. Sha, H. Zhu, Y. (Michael) Yang, *Joule* **2020**, *4*, 1594.
[13] G. E. Eperon, T. Leijtens, K. A. Bush, R. Prasanna, T. Green, J. T. W. Wang, D. P. McMeekin, G. Volonakis, R. L. Milot, R. May, A. Palmstrom, D. J. Slotcavage, R. A. Belisle, J. B. Patel, E. S. Parrott, R. J. Sutton, W. Ma, F. Moghadam, B. Conings, A. Babayigit, H. G. Boyen, S. Bent, F. Giustino, L. M. Herz, M. B. Johnston, M. D. McGehee, H. J. Snaith, *Science* **2016**, *354*, 861.
[14] D. Zhao, C. Chen, C. Wang, M. M. Junda, Z. Song, C. R. Grice, Y. Yu, C. Li, B. Subedi, N. J. Podraza, X. Zhao, G. Fang, R. G. Xiong, K. Zhu, Y. Yan, *Nat. Energy* **2018**, *3*, 1093.
[15] Q. Jiang, J. Tong, R. A. Scheidt, X. Wang, A. E. Louks, Y. Xian, R. Tirawat, A. F. Palmstrom, M. P. Hautzinger, S. P. Harvey, S. Johnston, L. T. Schelhas, B. W. Larson, E. L. Warren, M. C. Beard, J. J. Berry, Y. Yan, K. Zhu, *Science* **2022**, *378*, 1295.
[16] C. Wang, Y. Zhao, T. Ma, Y. An, R. He, J. Zhu, C. Chen, S. Ren, F. Fu, D. Zhao, X. Li, *Nat. Energy* **2022**, *7*, 744.
[17] X. Dai, S. Chen, H. Jiao, L. Zhao, K. Wang, Z. Ni, Z. Yu, B. Chen, Y. Gao, J. Huang, *Nat. Energy* **2022**, *7*, 923.
[18] Z. Yu, Z. Yang, Z. Ni, Y. Shao, B. Chen, Y. Lin, H. Wei, Z. J. Yu, Z. Holman, J. Huang, *Nat. Energy* **2020**, *5*, 657.
[19] R. He, W. Wang, Z. Yi, F. Lang, C. Chen, J. Luo, J. Zhu, J. Thiesbrummel, S. Shah, K. Wei, Y. Luo, C. Wang, H. Lai, H. Huang, J. Zhou, B. Zou, X. Yin, S. Ren, X. Hao, L. Wu, J. Zhang, J. Zhang, M. Stolterfoht, F. Fu, W. Tang, D. Zhao, *Nature* **2023**, *618*, 80.
[20] K. Xiao, Y. Lin, M. Zhang, R. D. J. Oliver, X. Wang, Z. Liu, X. Luo, J. Li, D. Lai, H. Luo, R. Lin, J. Xu, Y. Hou, H. J. Snaith, H. Tan, *Science* **2022**, *376*, 762.
[21] L. Li, Y. Wang, X. Wang, R. Lin, X. Luo, Z. Liu, K. Zhou, S. Xiong, Q. Bao, G. Chen, Y. Tian, Y. Deng, K. Xiao, J. Wu, M. I. Saidaminov, H. Lin, C. Q. Ma, Z. Zhao, Y. Wu, L. Zhang, H. Tan, *Nat. Energy* **2022**, *7*, 708.
[22] J. Tong, Z. Song, D. H. Kim, X. Chen, C. Chen, A. F. Palmstrom, P. F. Ndione, M. O. Reese, S. P. Dunfield, O. G. Reid, J. Liu, F. Zhang, S. P. Harvey, Z. Li, S. T. Christensen, G. Teeter, D. Zhao, M. M. Al-Jassim, M. F. A. M. Van Hest, M. C. Beard, S. E. Shaheen, J. J. Berry, Y. Yan, K. Zhu, *Science* **2019**, *364*, 475.
[23] A. F. Palmstrom, G. E. Eperon, T. Leijtens, R. Prasanna, S. N. Habisreutinger, W. Nemeth, E. A. Gaulding, S. P. Dunfield, M. Reese, S. Nanayakkara, T. Moot, J. Werner, J. Liu, B. To, S. T. Christensen, M. D. McGehee, M. F. A. M. van Hest, J. M. Luther, J. J. Berry, D. T. Moore, *Joule* **2019**, *3*, 2193.
[24] R. Lin, K. Xiao, Z. Qin, Q. Han, C. Zhang, M. Wei, M. I. Saidaminov, Y. Gao, J. Xu, M. Xiao, A. Li, J. Zhu, E. H. Sargent, H. Tan, *Nat. Energy* **2019**, *4*, 864.
[25] M. Wei, K. Xiao, G. Walters, R. Lin, Y. Zhao, M. I. Saidaminov, P. Todorović, A. Johnston, Z. Huang, H. Chen, A. Li, J. Zhu, Z. Yang, Y. K. Wang, A. H. Proppe, S. O. Kelley, Y. Hou, O. Voznyy, H. Tan, E. H. Sargent, *Adv. Mater.* **2020**, *32*, 1907058.
[26] K. Xiao, R. Lin, Q. Han, Y. Hou, Z. Qin, H. T. Nguyen, J. Wen, M. Wei, V. Yeddu, M. I. Saidaminov, Y. Gao, X. Luo, Y. Wang, H. Gao, C. Zhang, J. Xu, J. Zhu, E. H. Sargent, H. Tan, *Nat. Energy* **2020**, *5*, 870.
[27] R. Lin, J. Xu, M. Wei, Y. Wang, Z. Qin, Z. Liu, J. Wu, K. Xiao, B. Chen, S. M. Park, G. Chen, H. R. Atapattu, K. R. Graham, J. Xu, J. Zhu, L. Li, C. Zhang, E. H. Sargent, H. Tan, *Nature* **2022**, *603*, 73.
[28] B. A. Nejand, D. B. Ritzer, H. Hu, F. Schackmar, S. Moghadamzadeh, T. Feeney, R. Singh, F. Laufer, R. Schmager, R. Azmi, M. Kaiser, T. Abzieher, S. Gharibzadeh, E. Ahlswede, U. Lemmer, B. S. Richards, U. W. Paetzold, *Nat. Energy* **2022**, *7*, 620.
[29] Y. Wang, R. Lin, X. Wang, C. Liu, Y. Ahmed, Z. Huang, Z. Zhang, H. Li, M. Zhang, Y. Gao, H. Luo, P. Wu, H. Gao, X. Zheng, M. Li, Z. Liu, W. Kong, L. Li, K. Liu, M. I. Saidaminov, L. Zhang, H. Tan, *Nat. Commun.* **2023**, *14*, 1819.
[30] J. Zhu, Y. Luo, R. He, C. Chen, Y. Wang, J. Luo, Z. Yi, J. Thiesbrummel, C. Wang, F. Lang, H. Lai, Y. Xu, J. Wang, Z. Zhang, W. Liang, G. Cui, S. Ren, X. Hao, H. Huang, Y. Wang, F. Yao, Q. Lin, L. Wu, J. Zhang, M. Stolterfoht, F. Fu, D. Zhao, *Nat. Energy* **2023**, *8*, 714.
[31] L. Wagner, J. Suo, B. Yang, D. Bogachuk, E. Gervais, R. Pietzcker, A. Gassmann, J. C. Goldschmidt, arXiv:2306.13375, June, **2023**.
[32] R. Lin, K. Xiao, Z. Qin, Q. Han, C. Zhang, M. Wei, M. I. Saidaminov, Y. Gao, J. Xu, M. Xiao, A. Li, J. Zhu, E. H. Sargent, H. Tan, *Nat. Energy* **2019**, *4*, 864.
[33] H. Lai, J. Luo, Y. Zwirner, S. Olthof, A. Wieczorek, *Adv. Energy Mater.* **2022**, *12*, 2202438.
[34] J. Wen, Y. Zhao, Z. Liu, H. Gao, R. Lin, S. Wan, C. Ji, K. Xiao, Y. Gao, Y. Tian, J. Xie, C. J. Brabec, H. Tan, *Adv. Mater.* **2022**, *34*, 2110356.

[35] H. Chen, A. Maxwell, C. Li, S. Teale, B. Chen, T. Zhu, E. Ugur, G. Harrison, L. Grater, J. Wang, Z. Wang, L. Zeng, S. M. Park, L. Chen, P. Serles, R. A. Awni, B. Subedi, X. Zheng, C. Xiao, N. J. Podraza, T. Filleter, C. Liu, Y. Yang, J. M. Luther, S. Wolf, M. G. Kanatzidis, Y. Yan, E. H. Sargent, *Nature* **2022**, *613*, 676.
[36] Best Research-Cells Efficiencies, https://www.nrel.gov/pv/cell-efficiency.html, **November 2023**.
[37] M. A. Green, E. D. Dunlop, M. Yoshita, N. Kopidakis, K. Bothe, G. Siefer, X. Hao, *Prog. Photovoltaics* **2023**, *31*, 651.
[38] G. Kapil, T. Bessho, T. Maekawa, A. K. Baranwal, Y. Zhang, M. A. Kamarudin, D. Hirotani, Q. Shen, H. Segawa, S. Hayase, *Adv. Energy Mater.* **2021**, *11*, 2101069.
[39] G. Kapil, T. Bessho, C. H. Ng, K. Hamada, M. Pandey, M. A. Kamarudin, D. Hirotani, T. Kinoshita, T. Minemoto, Q. Shen, T. Toyoda, T. N. Murakami, H. Segawa, S. Hayase, *ACS Energy Lett.* **2019**, *4*, 1991.
[40] Z. Yang, Z. Yu, H. Wei, X. Xiao, Z. Ni, B. Chen, Y. Deng, S. N. Habisreutinger, X. Chen, K. Wang, J. Zhao, P. N. Rudd, J. J. Berry, M. C. Beard, J. Huang, *Nat. Commun.* **2019**, *10*, 1038.
[41] T. Zhou, H. Lai, T. Liu, D. Lu, X. Wan, X. Zhang, Y. Liu, Y. Chen, *Adv. Mater.* **2019**, *31*, 1901242.
[42] J. Tong, Q. Jiang, A. J. Ferguson, A. F. Palmstrom, X. Wang, J. Hao, S. P. Dunfield, A. E. Louks, S. P. Harvey, C. Li, H. Lu, R. M. France, S. A. Johnson, F. Zhang, M. Yang, J. F. Geisz, M. D. McGehee, M. C. Beard, Y. Yan, D. Kuciauskas, J. J. Berry, K. Zhu, *Nat. Energy* **2022**, *7*, 642.
[43] S. Hu, K. Otsuka, R. Murdey, T. Nakamura, M. A. Truong, T. Yamada, T. Handa, K. Matsuda, K. Nakano, A. Sato, K. Marumoto, K. Tajima, Y. Kanemitsu, A. Wakamiya, *Energy Environ. Sci.* **2022**, *15*, 2096.
[44] R. Lin, Y. Wang, Q. Lu, B. Tang, J. Li, H. Gao, Y. Gao, H. Li, C. Ding, J. Wen, P. Wu, C. Liu, S. Zhao, K. Xiao, Z. Liu, C. Ma, Y. Deng, L. Li, F. Fan, H. Tan, *Nature* **2023**, 994, https://doi.org/10.1038/s41586-023-06278-z.
[45] A. Rajagopal, R. J. Stoddard, S. B. Jo, H. W. Hillhouse, A. K. Y. Jen, *Nano Lett.* **2018**, *18*, 3985.
[46] I. Levine, O. G. Vera, M. Kulbak, D. R. Ceratti, C. Rehermann, J. A. Márquez, S. Levcenko, T. Unold, G. Hodes, I. Balberg, D. Cahen, T. Dittrich, *ACS Energy Lett.* **2019**, *4*, 1150.
[47] F. Peña-Camargo, P. Caprioglio, F. Zu, E. Gutierrez-Partida, C. M. Wolff, K. Brinkmann, S. Albrecht, T. Riedl, N. Koch, D. Neher, M. Stolterfoht, *ACS Energy Lett.* **2020**, *5*, 2728.
[48] A. Mahmud, J. Zheng, S. Tang, G. Wang, J. Bing, A. D. Bui, J. Qu, L. Yang, C. Liao, H. Chen, S. P. Bremner, H. T. Nguyen, J. Cairney, A. W. Y. Ho-baillie, *Adv. Energy Mater.* **2022**, *12*, 2201672.
[49] H. Lai, J. Luo, Y. Zwirner, S. Olthof, A. Wieczorek, F. Ye, Q. Jeangros, X. Yin, F. Akhundova, T. Ma, R. He, R. K. Kothandaraman, X. Chin, E. Gilshtein, A. Müller, C. Wang, J. Thiesbrummel, S. Siol, J. M. Prieto, T. Unold, M. Stolterfoht, C. Chen, A. N. Tiwari, D. Zhao, F. Fu, *Adv. Energy Mater.* **2022**, *12*, 202202438.
[50] F. Li, X. Deng, F. Qi, Z. Li, D. Liu, D. Shen, M. Qin, S. Wu, F. Lin, S. H. Jang, J. Zhang, X. Lu, D. Lei, C. S. Lee, Z. Zhu, A. K. Y. Jen, *J. Am. Chem. Soc.* **2020**, *142*, 20134.
[51] S. Mariotti, E. Köhnen, F. Scheler, K. Sveinbjörnsson, L. Zimmermann, M. Piot, F. Yang, B. Li, J. Warby, A. Musiienko, D. Menzel, F. Lang, S. Keßle, I. Levine, D. Mantione, A. Al-Ashouri, M. S. Härtel, K. Xu, A. Cruz, J. Kurpiers, P. Wagner, H. Köbler, J. Li, A. Magomedov, D. Mecerreyes, E. Unger, A. Abate, M. Stolterfoht, B. Stannowski, R. Schlatmann, et al., *Science* **2023**, *381*, 63.
[52] Method, computer program, and system for determining respective transport properties of majority as well as minority charge carriers in a sample, EP23173681.0 and DE102023112934.1.
[53] A. Musiienko, F. Yang, T. W. Gries, C. Frasca, A. Al-Ashouri, E. Sağlamkaya, F. Lang, D. Kojda, Y.-T. Huang, R. Hoye, M. Ahmadi, A. Kanak, A. Abate, *Res. Sq.* **2023**, https://doi.org/10.21203/rs.3.rs-3200897/v1.
[54] M. Jošt, L. Kegelmann, L. Korte, S. Albrecht, *Adv. Energy Mater.* **2020**, *10*, 1904102.
[55] K. Xu, A. Al-ashouri, Z. Peng, E. Köhnen, H. Hempel, F. Akhundova, J. A. Marquez, P. Tockhorn, O. Shargaieva, D. Abou-ras, F. Ruske, B. Stannowski, T. Unold, E. Unger, L. Korte, S. Albrecht, *ACS Energy Lett.* **2022**, *7*, 3600.
[56] J. Xu, C. C. Boyd, Z. J. Yu, A. F. Palmstrom, D. J. Witter, B. W. Larson, R. M. France, J. Werner, S. P. Harvey, E. J. Wolf, W. Weigand, S. Manzoor, M. F. A. M. Van Hest, J. J. Berry, J. M. Luther, Z. C. Holman, M. D. McGehee, *Science* **2020**, *367*, 1097.
[57] H. Uratani, K. Yamashita, *J. Phys. Chem. Lett.* **2017**, *8*, 742.
[58] J. Thiesbrummel, F. Peña-Camargo, K. O. Brinkmann, E. Gutierrez-Partida, F. Yang, J. Warby, S. Albrecht, D. Neher, T. Riedl, H. J. Snaith, M. Stolterfoht, F. Lang, *Adv. Energy Mater.* **2022**, *13*, 2202674.
[59] IR Spectrum Table & Charts, https://www.sigmaaldrich.com/US/en/technical-documents/technical-article/analytical-chemistry/photometry-and-reflectometry/ir-spectrum-table, **November 2023**.
[60] Y. Gao, H. Raza, Z. Zhang, W. Chen, Z. Liu, *Adv. Funct. Mater.* **2023**, *33*, 2215171.
[61] R. A. Belisle, K. A. Bush, L. Bertoluzzi, A. Gold-Parker, M. F. Toney, M. D. McGehee, *ACS Energy Lett.* **2018**, *3*, 2694.
[62] P. Caprioglio, S. Caicedo-Dávila, T. C. J. Yang, C. M. Wolff, F. Peña-Camargo, P. Fiala, B. Rech, C. Ballif, D. Abou-Ras, M. Stolterfoht, S. Albrecht, Q. Jeangros, D. Neher, *ACS Energy Lett.* **2021**, *6*, 419.
[63] D. Menzel, A. Tejada, A. Al-Ashouri, I. Levine, J. A. Guerra, B. Rech, S. Albrecht, L. Korte, *ACS Appl. Mater. Interfaces* **2021**, *13*, 43540.
[64] D. Menzel, A. Al-Ashouri, A. Tejada, I. Levine, J. A. Guerra, B. Rech, S. Albrecht, L. Korte, *Adv. Energy Mater.* **2022**, *12*, 2201109.
[65] Z. Hu, Z. Liu, L. K. Ono, M. Jiang, S. He, D. Y. Son, Y. Qi, *Adv. Energy Mater.* **2020**, *10*, 2000908.
[66] O. Gunawan, S. R. Pae, D. M. Bishop, Y. Virgus, J. H. Noh, N. J. Jeon, Y. S. Lee, X. Shao, T. Todorov, D. B. Mitzi, B. Shin, *Nature* **2019**, *575*, 151.
[67] Y. Chen, H. T. Yi, X. Wu, R. Haroldson, Y. N. Gartstein, Y. I. Rodionov, K. S. Tikhonov, A. Zakhidov, X. Y. Zhu, V. Podzorov, *Nat. Commun.* **2016**, *7*, 12253.
[68] J. Euvrard, O. Gunawan, D. B. Mitzi, *Adv. Energy Mater.* **2019**, *9*, 1902706.
[69] B. Krogmeier, F. Staub, D. Grabowski, U. Rau, T. Kirchartz, *Sustainable Energy Fuels* **2018**, *2*, 1027.
[70] Y. Zhao, K. Zhu, *J. Am. Chem. Soc.* **2014**, *136*, 12241.
[71] J. Tong, Q. Jiang, F. Zhang, S. B. Kang, D. H. Kim, K. Zhu, *ACS Energy Lett.* **2021**, *6*, 232.
[72] H. Shen, D. Walter, Y. Wu, K. C. Fong, D. A. Jacobs, T. Duong, J. Peng, K. Weber, T. P. White, K. R. Catchpole, *Adv. Energy Mater.* **2020**, *10*, 1902840.
[73] S. Gharibzadeh, B. Abdollahi Nejand, M. Jakoby, T. Abzieher, D. Hauschild, S. Moghadamzadeh, J. A. Schwenzer, P. Brenner, R. Schmager, A. A. Haghighirad, L. Weinhardt, U. Lemmer, B. S. Richards, I. A. Howard, U. W. Paetzold, *Adv. Energy Mater.* **2019**, *9*, 1803699.
[74] F. Yang, R. W. MacQueen, D. Menzel, A. Musiienko, A. Al-Ashouri, J. Thiesbrummel, S. Shah, K. Prashanthan, D. Abou-Ras, L. Korte, M. Stolterfoht, D. Neher, I. Levine, H. Snaith, S. Albrecht, *Adv. Energy Mater.* **2023**, *13*, 2204339.
[75] A. R. Bowman, F. Lang, Y. H. Chiang, A. Jiménez-Solano, K. Frohna, G. E. Eperon, E. Ruggeri, M. Abdi-Jalebi, M. Anaya, B. V. Lotsch, S. D. Stranks, *ACS Energy Lett.* **2021**, *6*, 612.
[76] Z. Yu, Z. Yang, Z. Ni, Y. Shao, B. Chen, Y. Lin, H. Wei, Z. J. Yu, Z. Holman, J. Huang, *Nat. Energy* **2020**, *5*, 657.
[77] P. Tockhorn, J. Sutter, A. Cruz, P. Wagner, K. Jäger, D. Yoo, F. Lang, M. Grischek, B. Li, J. Li, O. Shargaieva, E. Unger, A. Al-Ashouri, E. Köhnen, M. Stolterfoht, D. Neher, R. Schlatmann, B. Rech, B.

Stannowski, S. Albrecht, C. Becker, *Nat. Nanotechnol.* **2022**, *17*, 1214.

[78] F. Lang, E. Kohnen, J. Warby, K. Xu, M. Grischek, P. Wagner, D. Neher, L. Korte, S. Albrecht, M. Stolterfoht, *ACS Energy Lett.* **2021**, *6*, 3982.

[79] Y. Yang, C. Liu, A. Mahata, M. Li, C. Roldán-Carmona, Y. Ding, Z. Arain, W. Xu, Y. Yang, P. A. Schouwink, A. Züttel, F. De Angelis, S. Dai, M. K. Nazeeruddin, *Energy Environ. Sci.* **2020**, *13*, 3093.

[80] A. Onno, C. Chen, P. Koswatta, M. Boccard, Z. C. Holman, *J. Appl. Phys.* **2019**, *126*, 183103.